Monitoring electrode/electrolyte interfaces of Li-ion batteries under working conditions: A surface-enhanced Raman spectroscopic study on $LiCoO_2$ composite cathodes

Marcel Heber and Christian Hess*

Eduard-Zintl-Institute of Inorganic and Physical Chemistry, Technical University of Darmstadt, Alarich-Weiss-Str. 8, 64287 Darmstadt, Germany

*E-mail: christian.hess@tu-darmstadt.de

Abstract

Lithium-ion batteries are commonly used for electrical energy storage in portable devices and are promising systems for large-scale energy storage. However, their application is still limited due to electrode degradation and stability issues. To enhance the fundamental understanding of electrode degradation we report on the Raman spectroscopic characterization of $LiCoO_2$ cathode materials of working Li-ion batteries. To facilitate the spectroscopic analysis of the SEI (solid electrolyte interface) we apply surface-enhanced Raman spectroscopy by using Au nanoparticles coated with a thin SiO_2 layer ($Au@SiO_2$). We observe a surface-enhanced Raman signal of Li_2CO_3 at 1090 cm^{-1} during electrochemical cycling as an intermediate. Its formation/decomposition highlights the role of Li_2CO_3 as a component of the SEI on $LiCoO_2$ composite cathodes. Our results demonstrate the potential of Raman spectroscopy to monitor electrode/electrolyte interfaces of lithium-ion batteries under working conditions thus allowing relations between electrochemical performance and structural changes to be established.

Keywords: lithium batteries, solid electrolyte interface, $LiCoO_2$, *in situ* spectroscopy, Raman spectroscopy, SERS, SHINERS

1. Introduction

In light of the climate change and scarcity of fossil fuels, the topic of sustainable energy production and their usage becomes more and more relevant. In addition to the use of renewable energy sources, the storage of energy and the conversion of the transportation industry to electric vehicles represent important challenges for today's research, in which batteries play a key role. Among the rechargeable batteries, especially the lithium-ion battery is used in electronic devices [1]. The commercial lithium-ion battery contains e.g. $LiCoO_2$ as cathode material. Advantages of $LiCoO_2$ are its high specific capacity, low self-discharge, and high cycle life [2]. During the initial charging and discharging processes of the lithium-ion battery, a coating layer (SEI = solid electrolyte interface) forms on the electrode surface due to the reaction between the electrolyte and the cathode material, which may influence the capacity and life time of the battery [1,3]. A detailed characterization of the composition and formation processes of the top layer is therefore essential for the efficient use of lithium-ion batteries [4,5]. This layer is permeable to lithium ions and causes passivation of the electrode material [1], protecting it against further surface reactions and dendrite formation [6]. However, due to the formation of the SEI, some of the lithium ions are irreversibly lost. Furthermore, it represents an additional diffusion resistance, which can be speed-determining depending on the ion conductivity of the formed layer [7]. Reports on the chemical composition of the SEI include inorganic compounds such as Li_2O, LiF, and Li_2CO_3 [5,6], and organic compounds such as $ROCO_2Li$, ROLi, and LiOH [5,8-12]. There are several *ex situ* but only few *in situ* techniques available to study the electrode-electrolyte interface [5], such as XRR (X-ray reflectometry), NR (neutron reflectometry), and SERS (surface-enhanced Raman spectroscopy) [5,9,12]. For the characterization of the electrode material, Raman spectroscopy has proved to be a powerful method, as it can be performed without specific sample preparation and is suitable for

in situ measurements [5,13], thus allowing to monitor the dynamics inside the active material during the electrochemical process and to establish relations between electrochemical performance and structural changes. The literature describes a high temperature (HT) and a low temperature (LT) phase of $LiCoO_2$. In this study, HT-$LiCoO_2$ is used as a cathode material, which crystallizes in a hexagonal layer structure (space group $R\bar{3}m$) [14], consisting of a close-packed network of oxygen atoms with the Li^+ and Co^{3+} ions ordering on alternating (111) planes of the cubic rock-salt structure [15]. According to its space group, the irreducible representation is $A_{1g}+2A_{2u}+E_g+2E_u$, and the odd vibrational modes are Raman-inactive, while the straight modes are Raman active (A_{1g} and E_g) [13]. The first Raman study on $LiCoO_2$ was reported by Inaba *et al.* [16], in which the effect of the lithium content on the Raman-active bands was investigated, showing a reduction of the signal intensity due to deintercalation [16]. A disadvantage of normal Raman spectroscopy is its low sensitivity, which makes detection of the SEI layer difficult [17]. However, this issue can be resolved by using SERS [18], which provides a signal enhancement of up to six orders of magnitude [19] near rough Au, Ag or Cu surfaces [17], and has enabled identification of chemical species and detailed structural characterization in various research fields, including materials science, biosensing, catalysis, and electrochemistry [20]. Electrochemical electrodes are typically metal surfaces, allowing the direct application of SERS to study the behavior of adsorbed molecules [20-24], such as tetrathiafulvalene (TTF) derivatives extensively used in mechanostereochemistry and molecular electronic devices [20-22]. Using SHINERS, the SERS effect can be transferred to any sample surface, by coating metal nanoparticles with an inert shell such as SiO_2 or Al_2O_3 [25]. Hy *et al.* applied this approach to surface reactions on lithium-rich cathode materials ($Li[Ni_xLi_{(1-2x)/3}Mn_{(2-x)/3}]O_2$, $0 \leq x \leq 0.5$) during electrochemical cycling, and reported on the detection of intermediately formed Li_2O, leading to

Li_2CO_3 as a result of decomposition reactions of the electrolyte at the cathode [26]. Teshager *et al.* examined lithium-rich $Li_{1.2}Ni_{0.2}Mn_{0.6}O_2$ (LLNMO) and $LiCoO_2$ cathodes during first- and second-cycle charging and discharging with diffuse reflectance infrared Fourier-transformed spectroscopy (DRIFTS) while circulating the electrolyte [27]. This raises the question whether the conditions under electrolyte circulation can be compared to those of a conventional battery under working conditions. The authors reported various SEI species, e.g., RCOOR, Li_2CO_3, and $ROCO_2Li$, during charging above 4.0 and 4.5V and during discharging below 3.6 and 4.0 V for $LiCoO_2$ and LLNMO, respectively, attributed to EC decomposition [27]. In the context of Li-ion and Li-O_2 cells, Galloway *et al.* observed the formation of LiO_2, Li_2O_2, and Li_2CO_3 on lithium metal and planar carbon electrode interfaces, as well as on composite carbon black electrodes [28].

In this study, we use surface-enhanced Raman spectroscopy to study $LiCoO_2$ composite cathodes during electrochemical cycling. First, the synthesis and characterization of the shell-isolated Au@SiO_2 nanoparticles is presented. We then apply the nanoparticles to $LiCoO_2$ composite cathodes, allowing us to identify chemical species of the SEI layer and to monitor their dynamic behavior during electrochemical cycling.

2. Experimental section

2.1 Synthesis of the composite cathode

The synthesis of $LiCoO_2$ follows the Pechini process, which ensures a statistical distribution of the cations in the material [29]. $LiNO_3$ (Merck KGaA, ≥ 98 %), $Co(NO_3)_2$*$6H_2O$ (Merck KGaA, ≥ 99.0 %), and citric acid (AppliChem, ≥ 98%) are weighted and dissolved in water. A concentrated ammonia solution (25 %) is then added dropwise to the solution until the pH value is adjusted to

5. Ethylene glycol is added into the suspension and the temperature is set to 180 ℃ for six hours. The resulting black solid is first collected and ground, and then pre-calcined at 450 ℃ for six hours (heating rate: 1.5 ℃/min). The obtained brown powder is ground und calcined at 800 ℃ for 25 hours (heating rate: 20 ℃/min).

For the preparation of the composite cathode, the obtained $LiCoO_2$ is mixed with carbon black (TIMCAL, super p) and PVDF (Polyvinylidenfluorid, Solef, 6020/1001 H-6091) with a weight ratio of 84:8:8. By adding N-methyl-2-pyrrolidone (NMP) dropwise into the mixture, a thick flowing slurry is formed, which is then brushed on an aluminum net and dried overnight. The final material is cut into 12 mm round plates for insertion into the test cell.

2.2. Synthesis of $Au@SiO_2$

An aqueous solution of gold chloric acid ($HAuCl_4 \cdot 3H_2O$, Sigma-Aldrich, ≥ 99.9%) is refluxed in a three-necked flask. To the boiling solution 3% TSC ($Na_3C_6H_5O_7*2H_2O$, Sigma Aldrich, ≥ 99.9%) solution is added, and stirred for further 15 min under reflux. Then the solution is cooled to room temperature. PVP (Polyvinylpyrrolidon, Sigma Aldrich, MW = 40,000 g mol^{-1}) solution at a concentration of 12.8 mg/mL is added and stirred at room temperature overnight. After centrifuging, the sample is dispersed in water. The AuNP (gold nanoparticles) solution is added rapidly to a solution of anhydrous ethanol (Sigma-Aldrich, ≥ 99.8%), water, and 25 wt% NH_4OH solution.

For the preparation of coated gold nanoparticles ($Au@SiO_2$), 2.5 to 50 µl TEOS (Tetraethyl orthosilicate, Sigma Aldrich, ≥ 98%) in anhydrous ethanol is added to the solution. The solution is stirred for four hours at room temperature and then centrifuged. The residue is washed three

times with anhydrous ethanol. After each washing step, the solution is centrifuged again. The residue is dispersed in water.

2.3 Characterization of $Au@SiO_2$

The coated nanoparticles were checked for conformity by the gold catalyzed reduction of p-nitrophenol as an integral probe [30]. To this end, water, $NaBH_4$-solution (Merck), and 0.01 M p-nitrophenol are mixed in a cuvette. To this mixture, 100 µl of the nanoparticle solution is added and monitored by UV-VIS spectroscopy (Jasco V-770).

2.4 Raman spectroscopy

Raman experiments were performed by using 632 nm laser excitation from a diode laser (Ondax). The scattered light was sent to a transmission spectrometer (Kaiser Optical, HL5R) equipped with an electrically cooled CCD detector with 256×1024 pixels. The elastically scattered light was blocked by SuperNotch Plus filters (Kaiser Optical). For calibration of the spectrometer emission lines of standard Ne lamp were used. The spectral resolution was 5 cm^{-1}; the wavelength stability was better than 0.5 cm^{-1}. The laser power was set to 3.8 mW as measured at the position of the sample with a power meter (Ophir). The acquisition time for a single spectrum was 240 s, including the application of a cosmic ray filter and subtraction of the dark spectrum (laser off).

In situ Raman experiments were performed in a 180° backscattering geometry using a commercial test cell (EL Cell) [30] equipped with a glass optical window (see Figure 1). The battery cell consists of two electrodes separated by a layer of glass fiber filter paper soaked with electrolyte to prevent a short circuit.

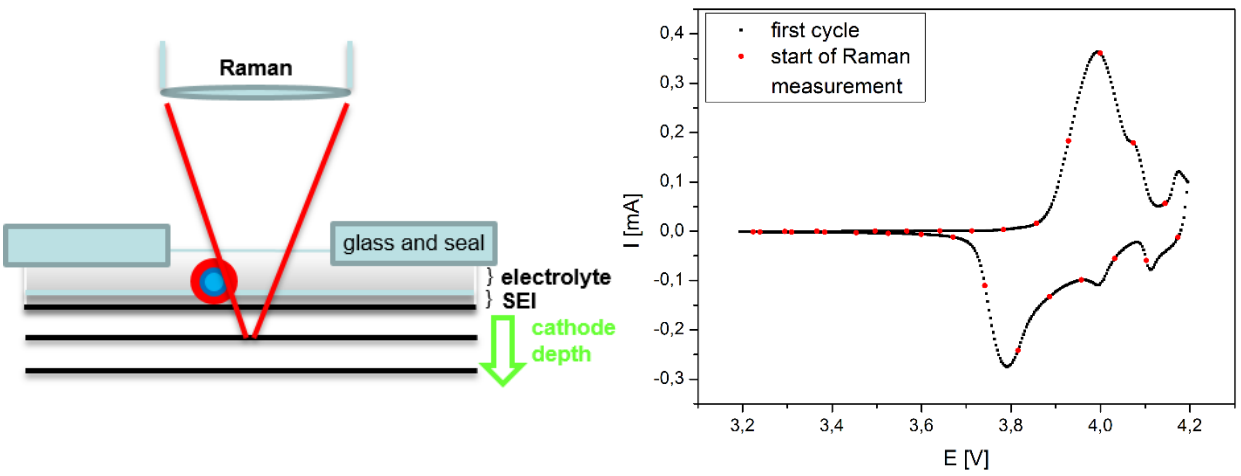

Figure 1. Left: *In situ* Raman spectroscopic analysis (632 nm) in the presence of $Au@SiO_2$ particles. Right: CV curve for the first cycle of the $LiCoO_2$ composite cathode. Metallic Li served as counter electrode and LP30 as electrolyte. Red points indicate the starting time of Raman measurements during cycling.

Cyclovoltammetric (CV) cycling was performed using a potentiostat from BioLogic (VSP). Metallic Li served as counter electrode at a cycling rate of 0.3 mV/s using potential limits of E_{min} = 3.2 V and E_{max} = 4.2 V. The electrolyte LP30 (Sigma-Aldrich, battery grade, impurities: < 50 ppm in HF, < 15 ppm H_2O) consisted of 1M $LiPF_6$ dissolved in ethylene carbonate and dimethyl carbonate (ratio 1:1). Raman spectra under quasi *in situ* conditions were recorded after six cycles. *In situ* Raman spectra were recorded continuously every four minutes during electrochemical cycling, as indicated in Figure 1. The CV profile of the *in situ* experiment is shown in the supporting information (see Figure S1). The test cell used for all Raman experiments made no observable contribution to the Raman signal. As part of the data analysis a least-square fit analysis was performed by using Voigt functions.

3. Results and discussion

For the analysis of the electrode/electrolyte interface we employ gold nanoparticles coated with SiO_2 ($Au@SiO_2$). Based on TEM images the gold nanoparticles possess an average diameter of 53 nm, whereas the thickness of the SiO_2 layer ranges between 5 and 34 nm (average: 29 nm). A TEM image of $Au@SiO_2$ nanoparticles employed in this study is shown in the left panel of Figure 2 (see inset).

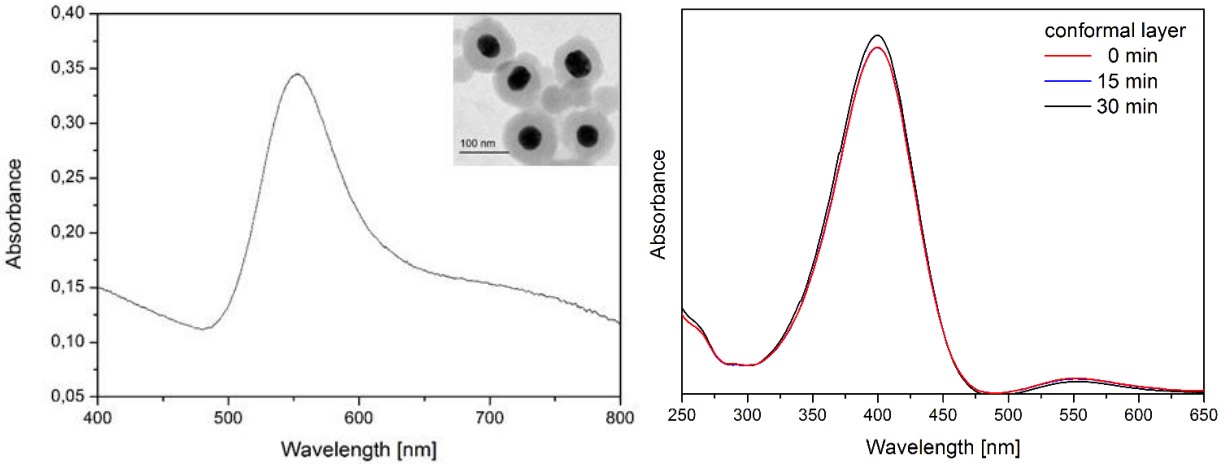

Figure 2. Left: UV-VIS spectrum of $Au@SiO_2$ solution. Inset: TEM image of $Au@SiO_2$ nanoparticles. Right: UV-VIS spectra of a p-nitrophenol solution with $Au@SiO_2$ particles used for the study.

The UV-VIS spectrum of the coated gold nanoparticles is characterized by absorption between 500 and 600 nm (see Figure 2), due to LSPR (localized surface plasmon resonance) excitation. For details of the synthesis and characterization of the $Au@SiO_2$ nanoparticles we refer to the experimental section and the supporting information (see SI, and Figures S2 and S3).

To check whether the coated nanoparticles are inert, the gold catalyzed reduction of p-nitrophenol was employed as an integral test reaction. For a non-conformal coating of the nanoparticles, the

accessible gold catalyzes the reduction of p-nitrophenol to p-phenylenediamine, i.e., the reduction of the nitro group, leading to a decrease of the absorption of the p-nitrophenol around 400 nm, and the appearance of product absorption at around 310 nm, as shown exemplarily in Figure S2 [31]. No conversion of p-nitrophenol was observed for the Au@SiO_2 nanoparticles employed in this study, as shown in the right panel of Figure 2.

The distance between the gold nanoparticles and the sample is determined by the thickness of the SiO_2 layer. The dependence of the surface-enhanced Raman signal on layer thickness was determined by Li *et al.* on the basis of the pyridine signal, which decreases with increasing layer thickness [25]. For a layer thickness of more than 10 nm, no signal enhancement was reported. We therefore assume those Au@SiO_2 particles with smaller layer thicknesses to contribute more strongly to the Raman intensity.

In the following, we will discuss the Raman spectra of the $LiCoO_2$ cathode material, first in the absence and then in the presence of Au@SiO_2 nanoparticles. The left panel of Figure 3 depicts the *ex situ* Raman spectrum of an as prepared $LiCoO_2$ composite cathode (yellow line), which is characterized by Raman bands of $LiCoO_2$ and carbon black. The Raman-active modes of $LiCoO_2$ result in signals at 486 cm^{-1} (E_g) and 597 cm^{-1} (A_{1g}) [34,35]. The broad bands at around 1340 cm^{-1} and 1600 cm^{-1} originate from carbon black in the composite cathode, and are attributed to the defect band (D) and to the C-C stretching mode of graphite (G), respectively [32,33]. The additive PVDF of the composite cathode does not give a contribution to the Raman spectrum of the as prepared cathode, as evidenced by comparison with the spectrum of bare PVDF (see Figure S4).

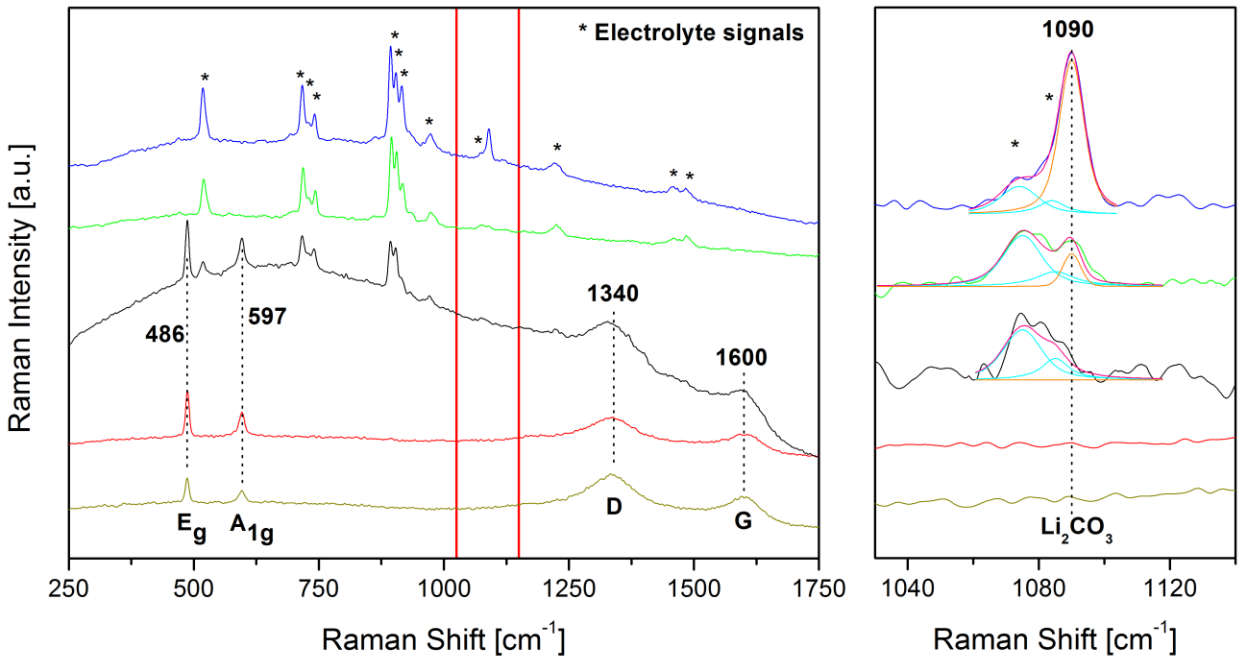

Figure 3. Left: *Ex situ* (yellow) Raman spectra of a $LiCoO_2$ composite cathode (84% $LiCoO_2$, 8% PVDF, 8% carbon black) and of a $LiCoO_2$ composite cathode with $Au@SiO_2$ particles (red). Quasi *in situ* Raman spectra of a cathode as assembled (black) and cycled (green). The blue spectrum corresponds to Li_2CO_3 and electrolyte (LP30) in the test cell without $Au@SiO_2$ particles. Right: Detailed view of the carbonate region of the Raman spectra (marked red in the left panel) after background subtraction together with the results of a fit analysis. Spectra were offset for clarity. Raman spectra were recorded with a 632 nm laser.

The $LiCoO_2$ composite cathode containing $Au@SiO_2$ nanoparticles is characterized by the red spectrum in Figure 3. Resembling the spectrum without $Au@SiO_2$ (yellow spectrum), Raman bands of $LiCoO_2$ and carbon black are detected. Please note that no additional signals are observed due to the presence of $Au@SiO_2$ particles, the additive PVDF of the composite cathode, or from any of the precursor compounds ($LiNO_3$, $Co(NO_3)_2$, PVP, TEOS, SiO_2,) (see Figures S5-S7).

In the presence of the electrolyte (LP30), additional electrolyte related Raman signals appear besides the $LiCoO_2$ and carbon related features (see black spectrum) [34,35]. The green spectrum recorded after six cyclovoltammetric cycles at a rate of 0.3 mV/s is dominated by electrolyte signals. It does not contain Raman features of the cathode material in this state of the sample due to the intercalation of the cathode, as described previously [16], and further supported by *in situ* Raman data during cycling (see Figures S8-S10). Besides, no Raman signals due to carbon black are observed, which is attributed to the heterogeneity of the composite cathode, displaying rearrangement on the surface of the composite cathode. In fact, comparison of Raman maps of $LiCoO_2$ composite cathode before and after electrochemical cycling show a redistribution of the chemical composition, due to a rearrangement of carbon additives, as described earlier [32,33]. Interestingly, upon cycling, changes are observed at around 1090 cm^{-1}, as indicated in the right panel of Figure 4. Based on a comparison with the spectrum of bare Li_2CO_3 (see Figures S11 and S12), we attribute the observed feature at 1090 cm^{-1} to the symmetric stretching vibration of carbonate in Li_2CO_3 [25,36]. As will discussed below, the presence of Li_2CO_3 indicates the formation or deposition of Li_2CO_3 on the composite cathode. As shown in the enlarged view of Figure 3, the presence of Li_2CO_3 is further supported by comparison with the Raman spectrum of a mixture of Li_2CO_3 and electrolyte (LP30) (see blue spectrum). Please note that the EC electrolyte possesses Raman signals at 1075 and 1085 cm^{-1} [35,37,38]. Thus, for a detailed analysis of this spectral region, all contributions need to be taken into account (see below). Nevertheless, our results demonstrate the presence of Li_2CO_3 as a component of the SEI after cycling and Raman analysis under quasi *in situ* conditions, i.e., after cycling without exposure to air.

To enhance the understanding of the dynamic behavior of Li_2CO_3 as a component of the SEI *in situ* surface enhanced Raman spectroscopy was applied directly under electrochemical conditions.

Figure 4 depicts *in situ* Raman spectra of the $LiCoO_2$ composite cathode with $Au@SiO_2$ particles during the first discharging process in the range of 3.4 V to 3.2 V and the second charging process in the range of 3.2 V to 3.4 V. The spectra are dominated by the Raman signals of the cathode and the electrolyte. During the discharge the cathode is intercalated and the E_g signal of $LiCoO_2$ increases. Additionally, as shown in the right panel of Figure 4, a dynamic behavior of the Li_2CO_3 signal at 1090 cm^{-1} is detected. The detailed view of the carbonate region of the Raman spectra shows the results of a least-square fit analysis of the carbonate Raman signal at 1090 cm^{-1} (orange) and Raman signals of EC (electrolyte) at 1085/1075 cm^{-1} (cyan) together with the resultant of all fit contributions (magenta). For details on the least-square fit analysis please refer to the Experimental section. Iinitially, no Li_2CO_3 signal is observed during electrochemical cycling, but during discharging the Li_2CO_3 signal emerges, and declines during the subsequent charging process. Please note that Li_2CO_3 has neither been observed in the assembled state of the composite cathode (see Figure 3, black spectrum), nor after storage of the assembled battery (see Figure S13). The integrated Raman signals are depicted in Figure 5. The Raman signal of Li_2CO_3 increases during the first discharging cycle, reaches a maximum at 3.2 V, and during the second charging decreases again (see Figures 4 and 5), until it disappears at 3.4 V. Beside the appearance of Li_2CO_3, no other additional Raman signals are observed during the *in situ* Raman measurements, e.g. from Li_2O or LiOH (see Figures S11 and S14). Also there is no indication for the formation of Co_3O_4, characterized by a signal at 691 cm^{-1} [39], suggesting degradation of $LiCoO_2$ [32].

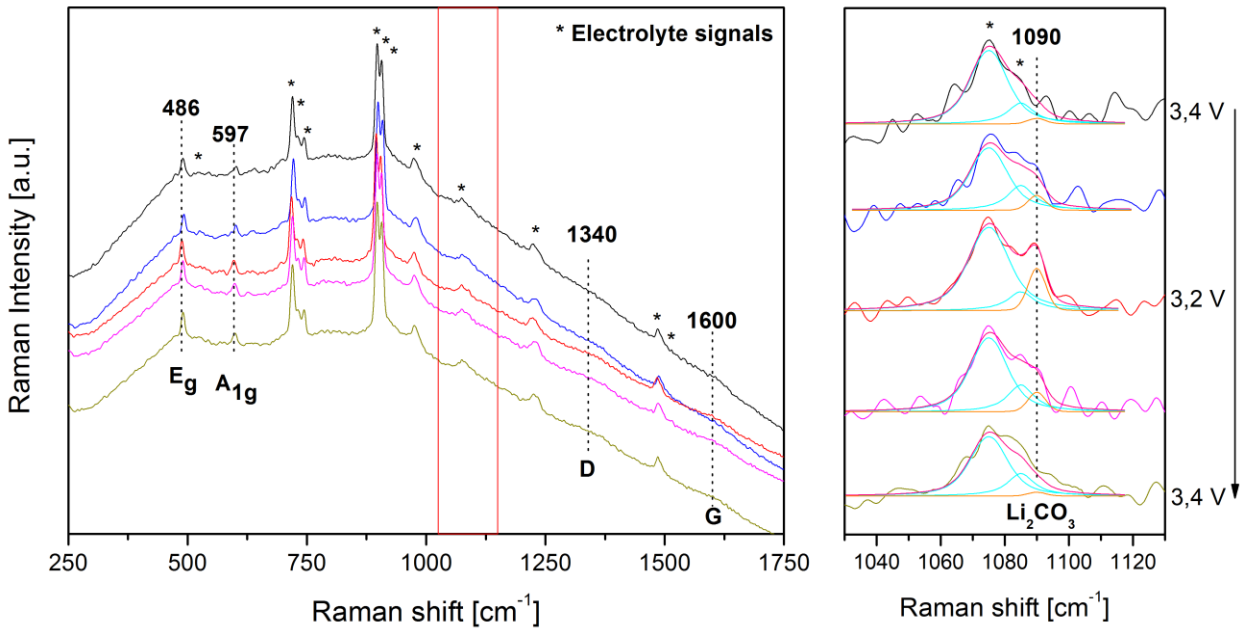

Figure 4. Left: *In situ* Raman spectra of a $LiCoO_2$ composite cathode (84% $LiCoO_2$, 8% PVDF, 8% carbon black) with Au@SiO_2 nanoparticles during the first discharging and second charging process using 632 nm laser excitation. Right: Detailed view of the carbonate region of the Raman spectra after background subtraction together with the results of a least-square fit analysis. Spectra were offset for clarity.

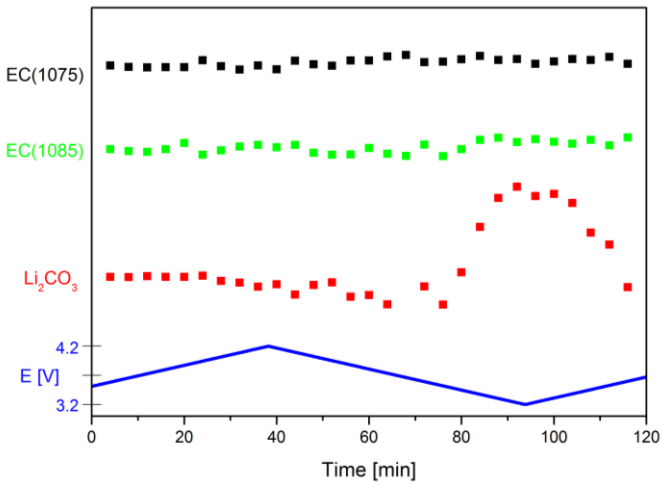

Figure 5. Integrated Raman signals of Li_2CO_3 (1090 cm^{-1}, red points) and EC (1085 cm^{-1}, green points, and 1075 cm^{-1}, black points) during the first charging, first discharging, and second charging process (blue line). The signals are the result of a least-square fit analysis of the spectra shown in Figures 4 and S8.

Turning to the discussion of the mechanism, the composition of Li_2CO_3 may proceed via different reaction pathways. One possible scenario is based on the reduction of EC and DMC, and the formation of lithium-alkyl compounds (see eq. 1). Li_2CO_3 may be formed starting from $(CO_3Li)^-$ (see eq. 2) [8,10,11,40-42]. Intermediately formed Li_2O may also react to Li_2CO_3 (see eq. 3) [26].

$$(CH_2O)_2CO + 2e^- + Li^+ \rightarrow C_2H_4 + (CO_3Li)^- \quad (1)$$

$$(CO_3Li)^- + Li^+ \rightarrow Li_2CO_3 \quad (2)$$

$$Li_2O + CO_2 \rightarrow Li_2CO_3 \quad (3)$$

$$H_2O + e^- + Li^+ \rightarrow LiOH + ½\ H_2 \quad (4)$$

$$LiOH + e^- + Li^+ \rightarrow Li_2O + ½\ H_2 \quad (5)$$

$$(CH_2OCO_2Li)_2 + H_2O \rightarrow Li_2CO_3 + CO_2 + (CH_2OH)_2 \quad (6)$$

$$2\ CO_2 + 2e^- + 2\ Li^+ \rightarrow Li_2CO_3 + CO \quad (7)$$

$$2\ HF + Li_2CO_3 \rightarrow 2\ LiF + H_2O + CO_2 \quad (8)$$

Traces of water can also produce LiOH, Li_2O, and Li_2CO_3 (see eqs. 4-6) [6]. Furthermore, CO and CO_2 formed at the beginning of discharging may also react to Li_2CO_3 (see eq. 7) [6,43]. However, our results indicate the formation of Li_2CO_3 from a lithium-alkyl compound, as no signals of LiOH or Li_2O are detected, in contrast to previous proposals based on *ex situ* experiments, underlining the importance of direct analysis under electrochemical conditions.

Previously, Hy *et al.* observed the formation of Li_2CO_3 on LLNMO cathodes during discharging, while intermediately formed Li_2O was observed during charging [26]. It was proposed that

LLNMO materials release oxygen to form Li_2O by charge compensation through a combination of $Ni^{2+/4+}$ and $Mn^{3+/4+}$ redox couples. While the authors applied a similar approach to prepare the composite cathode using carbon black and PVDF, a graphite anode was employed as counter electrode and 1M $LiPF_6$ in EC/DEC (ratio 1:1) as electrolyte. Besides, Teshager *et al.* reported the formation of Li_2CO_3 on $LiCoO_2$ cathodes during charging above 4.0 V and during discharging below 3.6 V [27]. The authors proposed the decomposition of the EC electrolyte. However, the assigned signals of Li_2CO_3 are different to those published previously from the same group [44]. On the experimental side, the charging potential of 4.5 V was above the electrochemical window (< 4.3 V) of the electrolyte and cathode, and the circulation of electrolyte differed from a diffusive behaviour of a conventional battery under working conditions. The decomposition of Li_2CO_3 could be induced electrochemically at higher potential. Hong *et al.* observed FTIR signals of Li_2CO_3 appearing and disappearing repeatedly with discharging and charging on Li-excess metal oxides ($Li_{1.2}Ni_{0.2}Mn_{0.6}O_2$) [43]. According to the authors, Li_2CO_3 decomposed to CO and CO_2 during charging, as supported by DEMS (differential electrochemical mass spectroscopy) during the charging steps. Besides, Li_2CO_3 may undergo reactions further, e.g. to LiF (see eq. 8) [43]. HF may be present in the electrolyte due to impurities or decomposition of $LiPF_6$. LiF could also be formed by decomposition of $LiPF_6$ [6,43,45]. LiF should be more resistive than carbonates in the electrolytic environment [8,46]. Due to changes of the chemical composition of the composite cathode during electrochemical cycling as discussed previously [32,33], a rearrangement of Li_2CO_3 on the surface is possible.

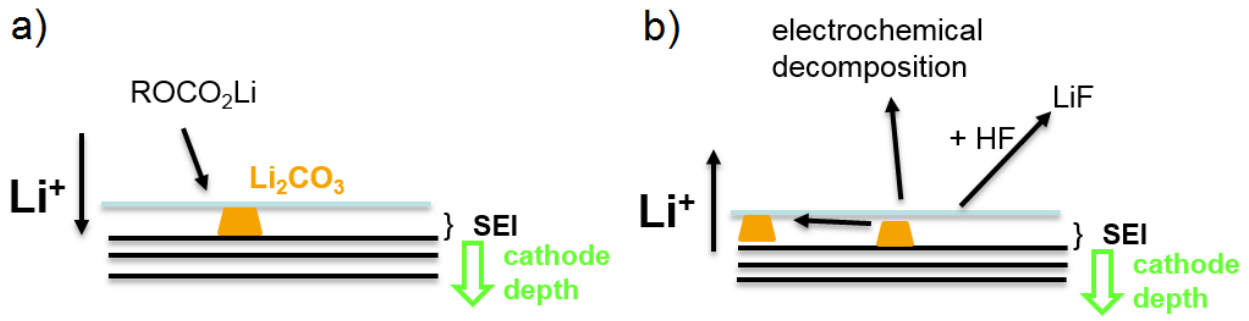

Figure 6. Proposed pathways for (a) Li_2CO_3 formation during discharging and (b) Li_2CO_3 decomposition during charging. For details see text.

The proposed pathway of the composition/decomposition of Li_2CO_3 on a $LiCoO_2$ composite cathode is illustrated in Figure 6. Based on our findings we propose a reaction pathway for the formation of Li_2CO_3 from lithium-alkyl compounds. Li_2CO_3 decomposition may proceed via several pathways as discussed above, e.g. by further reaction to LiF, and/or electrochemical decomposition to CO and CO_2. The decline of the carbonate Raman signal may also be due to a rearrangement of the surface during electrochemical cycling. In contrast to the results by Hy *et al.* for LLNMO materials [26], our Raman results suggest that for $LiCoO_2$ composite cathodes other reaction pathways are operative during formation/decomposition of Li_2CO_3, highlighting the role of the cathode composition. In fact, our findings suggest that the SEI formation originates from electrolyte decomposition. On the other hand, in the presence of Ni or Mn, the cathode material appears to be more reactive than $LiCoO_2$, thus opening different reaction pathways.

4. Conclusions

To increase the sensitivity of *in situ* Raman spectroscopy for monitoring Li-ion batteries under working conditions, surface-enhanced Raman spectroscopy was applied by using coated gold nanoparticles. Gold nanoparticles were prepared starting from gold chloric acid, coated with SiO_2 ($Au@SiO_2$), and checked for conformity by a gold catalyzed test reaction.

Ex situ and quasi *in situ* Raman spectra of cycled $LiCoO_2$ composite cathodes, recorded in the presence of $Au@SiO_2$ nanoparticles, showed a carbonate signal at 1090 cm^{-1}, besides the signals of the active material ($LiCoO_2$) and the electrolyte, indicating the formation of Li_2CO_3. Raman experiments under working conditions confirm the formation of Li_2CO_3 during electrochemical cycling. Detailed analysis reveals the formation and decomposition of Li_2CO_3, highlighting its role as an intermediate of the SEI. The formation of Li_2CO_3 is proposed to proceed via electrolyte reduction. The disappearance of the Li_2CO_3 signal may occur via different pathways, e.g. by reaction to LiF, or electrochemical decomposition, and may also proceed via rearrangement on the surface of the cathode. Our results indicate that Li_2CO_3 is an intermediate and a component of the SEI on a $LiCoO_2$ composite cathode. Thus, our analysis of the $LiCoO_2$ composite cathode demonstrates the potential of in situ/operando Raman spectroscopy to provide new insight into the SEI formation during operation of Li-ion batteries.

The dynamical aspects of the SEI are highly relevant to the discussion of electrode degradation. To extend the knowledge gained for $LiCoO_2$ composite cathodes, as a next step, the Raman approach could be applied to more complex cathode materials of NMC-type. To further enhance the understanding of the SEI formation on cathode materials, it would also be interesting to systematically introduce Mn and Ni to the composite cathodes, exchanging Co with Mn and/or Ni, in the future.

Supporting Information

Details on the synthesis and coating of the gold nanoparticles; Supporting cyclic voltammogram, Raman spectra, and UV-VIS spectra.

Notes

The authors declare no competing financial interest.

Acknowledgments

This work was supported by the Deutsche Forschungsgemeinschaft (DFG, HE 4515/8-1). The authors thank Dr. S. Lauterbach from the group of Prof. Dr. H.-J. Kleebe (TU Darmstadt) for performing the TEM measurements.

Notes and References

[1] Etacheri, V.; Marom, R.; Elazari, R.; Salitra, G.; Aurbach, D. Challenges in the development of advanced Li-ion batteries: A review. *Energy Environ. Sci*. **2011,** 4, 3243-3262.

[2] Antolini, E. $LiCoO_2$: formation, structure, lithium and oxygen nonstoichiometry, electrochemical behaviour and transport properties. *Solid State Ion*. **2004,** 170, 159-171.

[3] Hausbrand, R.; Cherkashinin, G.; Ehrenberg, H.; Gröting, M.; Albe, K.; Hess, C.; Jaegermann, W. Fundamental degradation mechanisms of layered oxide Li-ion battery cathode materials: methodology, insights and novel approaches. *Mater. Sci. Eng. B.* **2015**, 192, 3-25.

[4] Vetter, J.; Novák, P.; Wagner, M. R.; Veit, C.; Möller, K.-C.; Besenhard, J.O.; Winter, M.; Wohlfahrt-Mehrens, M.; Vogler, C.; Hammouche, A. Ageing mechanisms in lithium-ion batteries. *J. Power Sources*. **2005**, 147, 269-281.

[5] Tripathi, A. M.; Su, W.-N.; Hwang, B. J. *In situ* analytical techniques for battery interface analysis. *Chem. Soc. Rev*. **2018,** 47, 736-851.

[6] Aurbach, D. Review of selected electrode-solution interactions which determine the performance of Li and Li ion batteries. *J. Power Sources* **2000,** 89, 206-218.

[7] Edström, K.; Gustafsson T.; Thomas J. O. The cathode-electrolyte interface in the Li-ion battery. *Electrochim. Acta*. **2004,** 50, 397-403.

[8] Aurbach, D.; Zinigrad, E.; Cohen, Y.; Teller, H. A short review of failure mechanisms of lithium metal and lithiated graphite anodes in liquid electrolyte solutions. *Solid State Ion.* **2002,** 148, 405-416.

[9] Peled, E.; Menkin, S. Review – SEI: past, present and future. *J. Electrochem. Soc*. **2017**, 164, A1703-A1719.

[10] Aurbach, D.; Zaban, A.; Gofer, Y.; Ely, Y. E.; Weissman, I.; Chusid, O.; Abramson, O. Recent studies of the lithium-liquid electrolyte interface electrochemical, morphological and spectral studies of a few important systems. *J. Power Sources* **1995,** 54, 76-84.

[11] Aurbach, D.; Markovsky, B.; Levi, M. D.; Levi, E.; Schechter, A.; Moshkovich, M.; Cohen, Y. New insights into the interactions between electrode materials and electrolyte solutions for advanced nonaqueous batteries. *J. Power Sources* **1999,** 81-82, 95-111.

[12] Verma, P.; Maire, P.; Novák, P. A review of the features and analyses of the solid electrolyte interphase in Li-ion batteries. *Electrochim. Acta*. **2010**, 55, 6332-6341.

[13] Baddour-Hadjean, R.; Pereira-Ramos, J.-P. Raman microspectrometry applied to the study of electrode materials for lithium batteries. *Chem. Rev*. **2010,** 110, 1278-1319.

[14] Palacin, M. R. Recent advances in rechargeable battery materials: a chemist's perspective. *Chem. Soc. Rev*. **2009**, 38, 2565-2575.

[15] Reimers, J. N.; Dahn, J. R. Electrochemical and *in situ* X-ray diffraction studies of lithium intercalation in Li_xCoO_2. *J. Electrochem. Soc*. **1992**, 139, 8, 2091-2097.

[16] Inaba, M.; Iriyama, Y.; Ogumi, Z.; Todzuka, Y.; Tasaka, A. Raman study of layered rock-salt $LiCoO_2$ and its electrochemical lithium deintercalation. *J. Raman Spectrosc*. **1997**, *28*, 613-617.

[17] Anema, J. R.; Li, J.-F.; Yang, Z.-L.; Ren, B.; Tian, Z.-Q. Shell-isolated nanoparticle-enhanced raman spectroscopy: expanding the versatility of surface-enhanced Raman scattering. *Annu. Rev. Anal. Chem*. **2011,** 4, 129-150.

[18] Fleichschmann, M.; Hendra, P. J.; McQuillan, A. J. Raman spectra of pyridine adsorbed at a silver electrode. *Chem. Phys. Lett*. **1974,** 26, 163-166.

[19] Stiles, P. L.; Dieringer, J. A.; Shah, N. C.; Van Duyne, R. P. Surface-enhanced Raman spectroscopy. *Annu. Rev. Anal. Chem*. **2008,** 1, 601-626.

[20] Sharma, B.; Frontiera, R. R.; Henry, A.-I.; Ringe, E.; Van Duyne, R. P. SERS: materials, applications, and the future. *Mater. Today* **2012**, 15, 16-25.

[21] Flood, A. H.; Stoddart, J. F.; Steuerman, D. W.; Heath, J. R. Whence molecular electronics. *Science* **2004**, 306, 2055-2056.

[22] Olson, M. A.; Botros, Y. Y.; Stoddart, J. F. Mechanostereochemistry. *Pure Appl. Chem*. **2010**, 82, 1569-1574.

[23] Van Duyne, R. P.; Haushalter, J. P. Resonance Raman spectroelectrochemistry of semiconductor electrodes: the photooxidation of tetrathiafulvalene at n-GaAs(100) in acetonitrile. *J. Phys. Chem*. **1984**, 88, 2446-2451.

[24] Paxton, W. F.; Kleinman, S. I.; Basuray, A. N.; Stoddart, J. F.; Van Duyne, R. R. Surface-enhanced Raman spectroelectrochemistry of TTF-modified self-assembled monolayers. *J. Phys. Chem. Lett*. **2011**, 2, 1145-1149.

[25] Li, J. F.; Huang, Y. F.; Ding, Y.; Yang, Z. L.; Li, S. B.; Zhou, X. S.; Fan, F. R.; Zhang, W.; Zhou, Z. Y.; Wu, D. Y.; Ren, B.; Wang, Z. L.; Tian, Z. Q. Shell-isolated nanoparticle-enhanced Raman spectroscopy. *Nature* **2010,** 464, 392-395.

[26] Hy, S.; Felix, F.; Rick, J.; Su, W.-N.; Hwang, B. J. Direct *in situ* observation of Li_2O evolution on Li-rich high-capacity cathode material, $Li[Ni_xLi_{(1-2x)/3}Mn_{(2-x)/3}]O_2$ ($0 \leq x \leq 0.5$). *J. Am. Chem. Soc*. **2014**, 136, 999-1007.

[27] Teshager, M. A.; Lin, S. D.; Hwang, B.-J.; Wang, F.-M.; Hy, S.; Haregewoin, A. M. In situ DRIFTS analysis of solid-electrolyte interphase formation on Li-rich $Li_{1.2}Ni_{0.2}Mn_{0.6}O_2$ and

$LiCoO_2$ cathodes during oxidative electrolyte decomposotion. *ChemElectroChem.* **2016**, 3, 337-345.

[28] Galloway, T. A.; Cabo-Fernandez, L.; Aldous, I. M.; Braga, F.; Hardwick, L. J. Shell isolated nanoparticles for enhanced Raman spectroscopy studies in lithium-oxygen cells. *Faraday Disc.* **2017**, 205, 469-490.

[29] Pechini, P. M. Method of preparing lead and alkaline earth titanates and niobates and coating method using the same to form a capacitor. US Patent Nr. 3.330.697, **1967**.

[30] Radtke, M; Hess, C. Operando Raman shift replaces current in electrochemical analysis of Li-ion batteries: A comparative study. *Molecules* **2021**, 26, 4667.

[31] Zhao, Y.; Yang, D.; Hu, H.; Chen, L.; Xu, Y.; Qu, L.; Yang, P.; Zhang, Q. A simple approach to the synthesis of eccentric $Au@SiO_2$ janus nanostructures and their catalytic applications. *Surf. Sci*. **2016,** 648, 313-318.

[32] Gross, T.; Hess, C. Spatially-resolved in situ Raman analysis of $LiCoO_2$ electrodes. *ECS Trans.* **2014**, 63, 137-144.

[33] Gross, T.; Hess, C. Raman diagnostics of $LiCoO_2$ electrodes for lithium-ion batteries, *J. Power Sources* **2014**, 256, 220-225.

[34] By comparison of the Raman signals of the electrolyte from the black spectrum in the presence of $Au@SiO_2$ nanoparticles and the blue spectrum in the absence of $Au@SiO_2$ nanoparticles (see Figure 2), no shift of the Raman signals of the electrolyte is observed due to adsorption on bare gold particles. This is a further indication of the conformity of the $Au@SiO_2$ particles [35].

[35] Yang, G.; Ivanov I. N.; Ruther, R. E.; Sacci, R. I.; Subjakova, V.; Hallinan, D. T.; Nanda, J. Electrolyte solvation structure at solid-liquid interface probed by nanogap surface-enhanced Raman spectroscopy. *ACS Nano* **2018**, 12, 10159-10170.

[36] Koura, N.; Kohara, S.; Takeuchi, K.; Takahashi, S.; Curtiss, L. A.; Grimsditch, M.; Saboungi, M.-L. Alkali carbonates: Raman spectroscopy, ab initio calculations, and structure. *J. Mol. Struct*. **1996**, 382, 163-169.

[37] Fortunato, B.; Mirone, P.; Fini, G. Infrared and Raman spectra and vibrational assignment of ethylene carbonate. *Spectrochim. Acta A Mol. Biomol. Spectrosc.* **1971**, 27A, 1917-1927.

[38] Chen, D.; Mahmoud, M. A.; Wang, J.-H.; Waller, G. H.; Zhao, B.; Qu, C.; El-Sayed, M. A.; Liu, M. Operando investigation into dynamic evolution of cathode-electrolyte interfaces in a Li-ion battery. *Nano Lett*. **2019**, 19, 2037-2043.

[39] Hadjiev, V. G.; Iliev, M. N.; Vergilov, I. V. The Raman spectra of Co_3O_4. *J. Phys. C: Solid State Phys*. **1988,** 21, L199-L201.

[40] Wang, Y.; Nakamura, S.; Ue, M.; Balbuena, P. B. Theoretical studies to understand surface chemistry on carbon anodes for lithium-ion batteries: reduction mechanisms of ethylene carbonate. *J. Am. Chem. Soc.* **2001**, 123, 11708-11718.

[41] Herstedt, M.; Abraham, D. P.; Kerr, J. B.; Edström, K. X-ray photoelectron spectroscopy of negative electrodes from high-power lithium-ion cells showing various levels of power fade. *Electrochim. Acta* **2004**, 49, 5097-5110.

[42] Dedryvère, R.; Martinez, H.; Leroy, S.; Lemordant, D.; Bonhomme, F.; Biensan, P.; Gonbeau, D. Surface film formation on electrodes in a $LiCoO_2$/graphite cell: a step by step XPS study. *J. Power Sources* **2007**, 174, 462-468.

[43] Hong, J.; Lim, H.-D.; Lee, M.; Kim, S.-W.; Kim, H.; Oh, S.-T.; Chung, G.-C.; Kang, K. Critical role of oxygen evolved from layered Li-excess metal oxides in lithium rechargeable batteries. *Chem. Mater*. **2012**, 24, 2692-2697.

[44] Haregewoin, A. M.; Shie, T.-D.; Lin, S. D.; Hwang, B.-J.; Wang, F.-M. An effective in situ DRIFTS analysis of the solid electrolyte interface in lithium-ion battery. *ECS Trans.* **2013**, 53, 23–32.

[45] Tasaki, K.; Goldberg, A.; Lian, J.-J.; Walker, M.; Timmons, A.; Harris, S. J. Solubility of lithium salts formed on the lithium-ion battery negative electrode surface in organic solvents. *J. Electrochem. Soc.* **2009**, 156, A1019-A1027.

[46] Bi, Y.; Wang, T.; Liu, M.; Du, R.; Yang, W.; Liu, Z.; Peng, Z.; Liu, Y.; Wang, D.; Sun, X. Stability of Li_2CO_3 in cathode of lithium ion battery and its influence on electrochemical performance. *RSC Adv*. **2016**, 6, 19233-19237.